

# RSC Advances



This is an *Accepted Manuscript*, which has been through the Royal Society of Chemistry peer review process and has been accepted for publication.

*Accepted Manuscripts* are published online shortly after acceptance, before technical editing, formatting and proof reading. Using this free service, authors can make their results available to the community, in citable form, before we publish the edited article. This *Accepted Manuscript* will be replaced by the edited, formatted and paginated article as soon as this is available.

You can find more information about *Accepted Manuscripts* in the [Information for Authors](#).

Please note that technical editing may introduce minor changes to the text and/or graphics, which may alter content. The journal's standard [Terms & Conditions](#) and the [Ethical guidelines](#) still apply. In no event shall the Royal Society of Chemistry be held responsible for any errors or omissions in this *Accepted Manuscript* or any consequences arising from the use of any information it contains.



Journal Name

ARTICLE

## The *in-situ* prepared V<sub>2</sub>O<sub>5</sub>/graphene hybrid as superior cathode for lithium-ion batteries

Received 00th January 20xx,  
Accepted 00th January 20xx

DOI: 10.1039/x0xx00000x

www.rsc.org/

Mateti Srikanth, Md Mokhlesur Rahman\*, Lu Hua Li, Qiran Cai, Ying Chen\*

Developing the synthesis methods of graphene based cathode materials, with low cost and environmentally friendly way, is necessary for the industrial production. Although the precursor of graphene is abundant on the earth, the common precursor of graphene is graphene oxide (GO), needing many steps and reagents to transfer from graphite. The traditional approach for the synthesis of GO needs so many chemicals, leading to a high cost and potential damage to the environment. In this study, we develop a simple wet ball-milling method to construct V<sub>2</sub>O<sub>5</sub>/graphene hybrid structure in which nanometre-sized V<sub>2</sub>O<sub>5</sub> particles/aggregates are well embedded and uniformly dispersed into the crumpled and flexible graphene sheets generated by *in-situ* conversion of bulk graphite. The combination of V<sub>2</sub>O<sub>5</sub> nanoparticles/aggregates and *in-situ* graphene leads the hybrid to exhibit markedly enhanced discharge capacity, excellent rate capability, and good cycling stability. This study suggests that nanostructured metal oxide electrodes in integration with graphene can address the poor cycling issues of electrode materials that suffer from low electronic and ionic conductivities. This simple wet ball-milling method can potentially be used to prepare various graphene based hybrid electrodes for large scale energy storage applications.

### Introduction

Lithium-ion batteries (LIBs) power most portable electronic devices and are regarded as the potential power source for electric vehicles (EVs) and hybrid electric vehicles (HEVs). To meet the requirements for widespread use in EVs and HEVs, LIBs with satisfactory high energy and power densities, safety, and cycling stability must be developed.<sup>1</sup> Therefore, there is an urgent need to develop high-performance electrode materials for next-generation LIBs. In LIBs, the cathode is typically a metal oxide and serves as the host for Li<sup>+</sup> ion intercalation during the charge/discharge process. A variety of compounds have already been tested, and some of them have been used commercially as cathode materials for the manufacture of lithium ion batteries.<sup>2</sup> Among the commonly used cathode materials such as LiCoO<sub>2</sub> (274 mA h g<sup>-1</sup>)<sup>3</sup> and LiFePO<sub>4</sub> (170 mA h<sup>-1</sup>),<sup>4</sup> vanadium pentoxide (V<sub>2</sub>O<sub>5</sub>) has a theoretical capacity of 294 mA h g<sup>-1</sup> when it is discharged to 2 V (vs. Li/Li<sup>+</sup>), which corresponds to two lithium intercalations.<sup>5</sup> Additionally, it is attractive as a cathode material for LIBs because of its low cost, abundance, easy synthesis, and high energy density.<sup>6,7</sup>

However, the practical application of V<sub>2</sub>O<sub>5</sub> in LIBs is greatly limited by several issues:<sup>8-11</sup> (i) low electronic conductivity, (ii) slow

lithium-ion diffusion, and (iii) irreversible phase transitions upon deep discharge. As a consequence, V<sub>2</sub>O<sub>5</sub> currently has very poor rate capability and very limited long-term cyclability. The rate capability of electrode materials is mainly determined by the kinetics of lithium-ion diffusion and electronic conductivity. Generally, the lithium-ion diffusion coefficient and the diffusion length are the two main factors which affect the rate of lithium-ion diffusion in the lattice of an electrode.<sup>12</sup> It is well known that the decrease in diffusion distance can effectively shorten the diffusion time of lithium ions within the electrode which is accompanied by nanomaterials during insertion/extraction, resulting in enhanced rate capability.<sup>13-15</sup> On the other hand, fast electron transport within the electrode also exerts a significant impact on the rate capability of LIBs. Electrode materials with low electronic conductivity produce resistance during cycling of the battery. As a result, the particle-particle interfaces became unfavourable for electron transportation which leads to unsatisfactory rate capability.<sup>2</sup>

To date, a significant effort has been focused on improving rate capability and cyclability of V<sub>2</sub>O<sub>5</sub> based cathode by overcoming intrinsic drawbacks of the materials. In particular, various nanostructured V<sub>2</sub>O<sub>5</sub> (for examples, nanoparticles, nanotubes, nanowires, nanorods, nanofibers, nanobelts, nano-rolls, nanosheets, porous microspheres, and porous microplates) have been synthesised to shorten the diffusion distance for Li<sup>+</sup> ions and buffer the volume change during the lithium intercalation and de-intercalation processes, as compared with bulk materials.<sup>9, 10, 16-25</sup>

Institute for Frontier Materials, Deakin University, Waurn Ponds, VIC 3216, Australia.

E-mail: m.rahman@deakin.edu.au; ian.chen@deakin.edu.au

Furthermore, these nanostructured  $V_2O_5$  are integrated with carbon nanomaterials (such as surface carbon coating, carbon nanotubes, and graphene) to ensure better cyclability during long term charge/discharge by facilitating faster electron transfer within the electrode.<sup>26-29</sup> These carbon nanomaterials not only enhance electrical conductivities of  $V_2O_5$  electrode films but also prevent agglomeration of nanostructured  $V_2O_5$  active materials during cycling.

As a kind of carbon materials, graphene has attracted much attention in the field of LIBs. Graphene is a single-atomic layer of  $sp^2$ -bonded carbon atoms arranged in a honeycomb crystal structure,<sup>30</sup> which provides extraordinary electrical, mechanical, and thermal properties.<sup>31</sup> Graphene can be prepared using either the chemical or thermal reduction of graphene oxide (GO),<sup>32</sup> which is a layered stack of oxidized graphene sheets with different functional groups. However, a common problem in preparing nanostructured  $V_2O_5$  based electrodes (such as nanostructured  $V_2O_5$  and corresponding hybrids of  $V_2O_5/C$ ,  $V_2O_5/CNTs$ ,  $V_2O_5/graphene$ ) is that most of the production methods are drastically different from existing industrial processes, and these methods are difficult to scale up for large-quantity production.<sup>2, 33-35</sup>

Herein, our comprehensive approach is to prepare  $V_2O_5/graphene$  hybrid electrode *via* an *in-situ* generation of graphene from graphite through ball milling technique, where bulk graphite and  $V_2O_5$  nanoparticles used as starting materials. By employing a simple procedure of mechanical milling, bulk graphite is converted to a few layers of graphene in presence of argon atmosphere and at the same time nanometre size  $V_2O_5$  particles and its aggregates are trapped and embedded among crumpled graphene sheets. Therefore, such a novel structure is expected to provide the intra-particle electronic conduction and the lithium-ion diffusion simultaneously. Furthermore, the use of nanometre size  $V_2O_5$  particles and its aggregates, in particular, helps to overcome the issues of ionic conductivity (by reducing the length scales for the ionic transport) and, to some extent, excessive stress developing in the electrode upon cycling. The hybrid we obtained exhibits markedly enhanced rate capability and excellent cycle ability when used as a cathode material for LIBs. To prepare a few-layer graphene materials from bulk graphite, mechanical ball milling is not only an inexpensive alternative approach, but also a powerful approach for *in-situ* formation of metal oxide/graphene hybrid with enhanced electrochemical properties for LIBs electrode.

## Experimental

### Preparation of $V_2O_5$ nanoparticles

To prepare  $V_2O_5$  nanoparticles, commercial  $V_2O_5$  (Sigma Aldrich,  $\geq 98\%$ ) was used as starting material. 4 g of commercial  $V_2O_5$  and four hardened steel balls with a diameter of 25.4 mm each were loaded in a stainless steel milling container. The milling container was then evacuated and purged with argon gas for 3 times, and finally it was filled with argon gas with starting pressure of 310 kPa. High energy ball in conjunction with an external magnet was used to mill commercial  $V_2O_5$  powders at a rotation speed of 160 rpm for 110 h. The milled  $V_2O_5$  powders were removed from the ball milling container in the presence of an inert argon atmosphere. The sample is known as  $V_2O_5$ -bm.

### In-situ preparation of $V_2O_5/graphene$ hybrid

Ball milled prepared  $V_2O_5$  nanoparticles ( $V_2O_5$ -bm) and crystalline graphite (particle size  $< 20 \mu m$ , Sigma Aldrich) powders were mixed in a 2:1 and 4:1 weight ratios. Both mixtures were loaded separately inside a stainless steel milling container together with four hardened steel balls (diameter of 25.4 mm) along with suitable amount of acetone as solvent. Both mixtures were milled in a rolling ball mill at a rotation speed of 75 rpm for 25 h at room temperature under an argon atmosphere of 100 kPa. Normally, bulk graphite is composed of numerous graphene flakes which are attached by the van der Waals attraction between adjacent graphene flakes. The ideal case is that graphene can be peeled from the bulk graphite layer by layer if the van der Waals attraction is minimised.<sup>36</sup> During ball milling, a shear force is generated when balls are moving. This dominating shear force is exerted in the lateral direction to overcome the van der Waals attraction and promote the relative motion between graphite layers, which leads to exfoliate graphite to graphene. On the other hand, the acetone solvent is used as an exfoliating agent to enhance the intercalation and promote exfoliation.<sup>37</sup> At the same time, dominating shear force also insert  $V_2O_5$  nanoparticles and its aggregate into the graphene sheets, and produce  $V_2O_5/graphene$  hybrid materials. Produced hybrids are denoted as  $V_2O_5/graphene$  (2:1) and  $V_2O_5/graphene$  (4:1), respectively. The overall preparation procedure is schematically presented in Fig. 1.

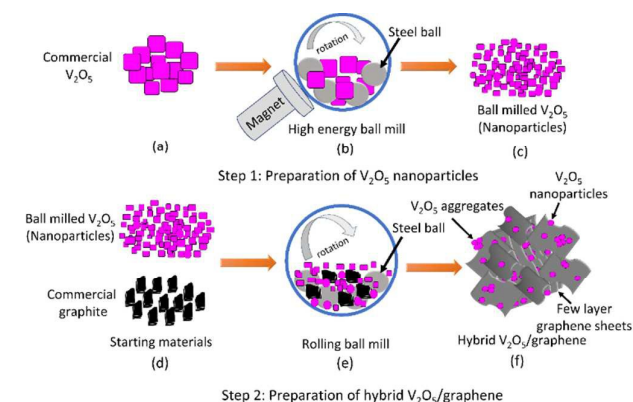


Fig. 1 Schematic illustration of materials preparation procedure.

### Material characterization

X-ray diffraction (XRD) data were collected from powder samples on a PANalytical X'Pert Powder instrument using a  $CuK\alpha$  radiation source ( $1.54 \text{ \AA}$ ) operated at 40 kV with 30 mA current. XRD data were recorded over a range of  $10\text{-}70^\circ$  with a step time and size of 150 s and 0.02, respectively. The X'Pert data collector software in combination with the Joint Committee on Powder Diffraction Standards (JCPDS) powder diffraction files was used to identify the phases present. Thermogravimetric analysis (TGA) was performed via a Q50 Thermogravimetric Analyzer in air to determine the actual amount of carbon in the hybrid samples. Transmission electron microscopy (TEM) investigations were performed using a JEOL JEM 2100F instrument operated at 200 kV. Raman spectroscopy

measurements were performed using a Renishaw in via micro-spectroscopic system. The laser used had a wavelength of 514 nm. The power was 0.5 mW to prevent the laser damage of the material. 20 X lens was used in the test. Each spectrum was accumulated from two scans. To test the electrochemical performance,  $V_2O_5$  and  $V_2O_5$ /graphene powder samples were mixed with acetylene carbon black (AB) and a binder, polyvinylidene fluoride (PVdF, Sigma-Aldrich), in a weight ratio of 80:10:10 in a solvent, N-methyl-2-pyrrolidone (NMP, Sigma-Aldrich, anhydrous, 99.5%). The as-prepared slurry was spread onto Al foil substrates with an average loading of 1.0-1.5 mg and these coated electrodes were dried in a vacuum oven at 100 °C for 12h. The electrode was then pressed using a 25 mm diameter disc to enhance the contact between the Al foil and active material. Subsequently, the electrodes were cut to 1x1 cm<sup>2</sup> and CR 2032 coin-type cells were assembled in an Ar-filled glove box. Li foil was used as the counter/reference electrode and a microporous polyethylene film was used as a separator. The electrolyte was 1 M LiPF<sub>6</sub> in a mixture of ethylene carbonate (EC), diethylene carbonate (DEC), and dimethyl carbonate (DMC) with a volume ratio of 1: 1: 1. The cells were galvanostatically discharged-charged in the range of 2.0-4.0 V at different current densities using a Land Battery Testing System (Wuhan LAND Electronics, Ltd. China). The temperature in the laboratory was maintained within a range of 20-25 °C during the tests. Cyclic voltammograms (CV) were recorded using Solartron Analytical electrochemical workstations at a scan rate of 0.05 mV s<sup>-1</sup>. Electrochemical impedance spectroscopy was performed on the cells over the frequency range of 100 kHz to 0.01 Hz using an Ivium-n-stat computer-controlled electrochemical analyser (Ivium Technologies, the Netherlands).

## Results and discussion

XRD patterns of the commercial  $V_2O_5$  sample ( $V_2O_5$ -cm) and three ball milled samples of  $V_2O_5$ -bm,  $V_2O_5$ /graphene (2:1), and  $V_2O_5$ /graphene (4:1) are shown in Fig. 2 (a). All the pronounced diffraction peaks for all samples can be indexed to an orthorhombic crystal system (JCPDS 04-007-6245, space group *Pmmn*, space group number 59) with lattice parameters of  $a = 3.5640 \text{ \AA}$ ,  $b = 11.5120 \text{ \AA}$ , and  $c = 3.8300 \text{ \AA}$ . However, it is observed that the XRD peaks of  $V_2O_5$ /graphene (4:1) sample are shifted to a higher angles which may be due to defects in crystals.<sup>38,39</sup> Low content of carbon (graphene) in  $V_2O_5$ /graphene (4:1) sample facilitates more friction and impact among  $V_2O_5$  particles and steel balls during milling. On the other hand, the friction and impact are minimised in  $V_2O_5$ /graphene (2:1) sample due the presence of large amount of carbon (graphene). As a results, more defects in crystals are expected in low carbon (graphene) content sample. The average crystallite sizes of the four samples are calculated using the Debye-Scherrer equation, where Si standard (111) peak is used as the full-width half-maximum (FWHM) reference. The average crystallite sizes are found to be 55, 57, 76, and 92 nm for  $V_2O_5$ -cm,  $V_2O_5$ -bm,  $V_2O_5$ /graphene (4:1), and  $V_2O_5$ /graphene (2:1) samples, respectively.

For quantifying the amount of carbon (graphene) in the hybrid samples, TGA analysis was carried out in air. The hybrid samples are heated from 100 to 950 °C at the rate of 5 °C min<sup>-1</sup>. As can be seen from Fig. 2 (b), both hybrid samples start to lose weight slowly

in air with increasing temperature, and maximum weight loss is found to take place around 350-650 °C. According to Fig. 2 (b), weight loss for the samples at 100-350 °C could be attributed to the loss of moisture and volatile organic compounds contained in the hybrids, whereas maximum weight loss at around 350-650 °C is corresponding to the amount of carbon (graphene). Therefore, the amount of carbon (graphene) in the hybrid samples can be estimated to be approximately 30 wt. % for  $V_2O_5$ /graphene (2:1) and 18 wt. % for  $V_2O_5$ /graphene (4:1), respectively.

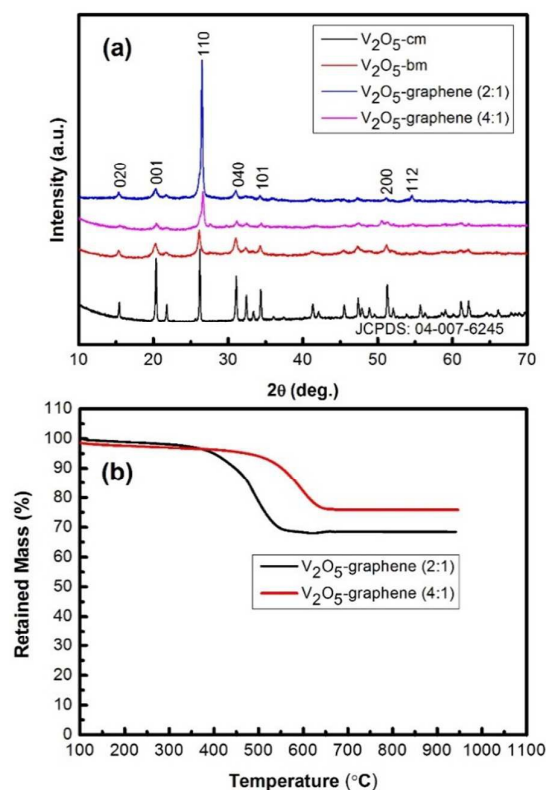


**Fig. 2** (a) XRD patterns of  $V_2O_5$ -cm,  $V_2O_5$ -bm,  $V_2O_5$ /graphene (2:1), and  $V_2O_5$ /graphene (4:1) samples; (b) TGA analysis of  $V_2O_5$ /graphene (2:1) and  $V_2O_5$ /graphene (4:1) samples.

The structure of each sample is visualised using TEM. Bright-field imaging of the  $V_2O_5$ -cm sample reveals flakes like morphology (Fig. 3 (a)). A dense agglomerates of  $V_2O_5$  nanoparticles is observed in ball milled  $V_2O_5$ -bm sample (Fig. 3 (b)). The corresponding selected area electron diffraction (SAED) pattern is also depicted in inset of the Fig. 3 (b). The SAED pattern consists of a single component of  $V_2O_5$  with  $d$  spacings of approximately 0.345, 0.198, and 0.1490 nm which can be referred to the crystallographic directions of (110), (051), and (170), respectively. These results are consistent with the XRD pattern obtained for this sample, as shown in Fig. 2 (a). Fig. 3 (c-f) display TEM bright field images of hybrid  $V_2O_5$ /graphene (2:1) (Fig. 3 (c, d)) and  $V_2O_5$ /graphene (4:1) (Fig. 3 (e, f)) samples, respectively. Corresponding selected area electron diffraction (SAED) patterns for both hybrids are depicted in inset of the Fig. 3 (c, e). TEM results clearly demonstrate the presence of wrinkles and

folds in the images which are characteristic features of graphene sheets (Fig. 3 (d, f)). To further confirm the characteristic features of graphene, Raman spectroscopy measurements are conducted (Fig. 9). The island-like  $V_2O_5$  nanoparticles/aggregates are dispersed on the surface of graphene sheets and encapsulated by few layer of graphene. Typically wrinkled graphene sheets form a network and cover the highly dispersed  $V_2O_5$  nanoparticles/aggregates which significantly increase conductivity and stabilize the cathode structure of the hybrid systems (Fig. 3 (d, f)). It is also found that  $V_2O_5$  nanoparticles/aggregates are not only anchored to graphene networks, but also trapped by few layer of graphene, which can ensure that most particles could contribute to the charge/discharge process.

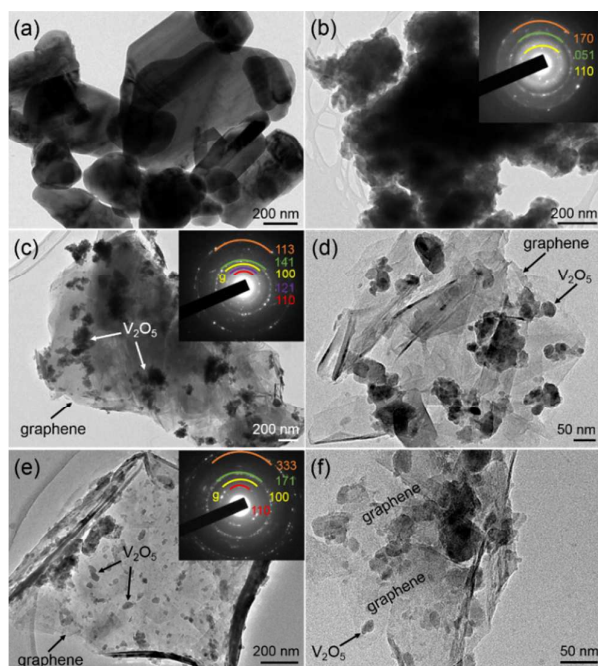
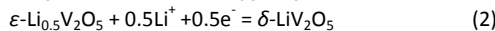


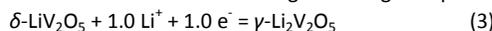
**Fig. 3** TEM characterization: (a) a bright-field image of  $V_2O_5$ -cm and (b) bright-field image and SAED pattern of  $V_2O_5$ -bm ; TEM images (c-f) of the hybrid samples: (c, d) images of hybrid  $V_2O_5$ /graphene (2:1) sample of (c) a bright-field image with SAED pattern and (d) magnified image of the local area of (c); (e, f) TEM images of hybrid  $V_2O_5$ /graphene (4:1) sample of (e) a bright-field image with SAED pattern and (f) magnified image of the local area of (e).

Cyclic voltammograms (CV) of the electrodes are measured at a scan rate of  $0.05 \text{ mV s}^{-1}$  in the potential range of 4.0-2.0 V (vs  $\text{Li}/\text{Li}^+$ ) (Fig. 4). This potential window is chosen to avoid the formation of irreversible  $\omega$ -phase of  $\text{Li}_x\text{V}_2\text{O}_5$  ( $2 < x < 3$ ) that occurs at deep depth of discharge.<sup>5</sup> In the CV curves, the cathodic and anodic peaks are ascribed to the lithium ion intercalation and de-intercalation processes for the electrodes, respectively. Three dominant cathodic peaks at the potentials of around 3.4, 3.1, and 2.2V are observed for all electrodes, which correspond to a series of phase transformation during lithium ion intercalation into the  $V_2O_5$  crystal with the formation of intercalation compounds of  $\epsilon\text{-Li}_{0.5}\text{V}_2\text{O}_5$ ,  $\delta\text{-LiV}_2\text{O}_5$ , and

$\gamma\text{-Li}_2\text{V}_2\text{O}_5$ , respectively.<sup>40, 41</sup> The cathodic peaks located at around 3.4 and 3.1V correspond to the intercalation of the first Li in two steps,



The second Li is inserted through one single step around 2.2V.



During anodic process, three anodic peaks observed at around 2.5, 3.2 and 3.4 V are ascribed to the two  $\text{Li}^+$  ions de-intercalation process and the corresponding reverse phase transformations from  $\gamma\text{-Li}_2\text{V}_2\text{O}_5$  to  $\delta\text{-LiV}_2\text{O}_5$ ,  $\epsilon\text{-Li}_{0.5}\text{V}_2\text{O}_5$ , and  $V_2O_5$  respectively, associated with the  $V^{4+}/V^{5+}$  redox couple [2, 8]. Apart from the main redox peaks, a pair of extra cathodic/anodic peaks at around 2.6/2.7V is observed for  $V_2O_5$ -bm,  $V_2O_5$ /graphene (2:1) and  $V_2O_5$ /graphene (4:1) electrodes. However, the pair of extra cathodic/anodic peaks is very obvious for the  $V_2O_5$ /graphene (4:1) electrode (compare to  $V_2O_5$ -bm and  $V_2O_5$ /graphene (2:1) electrodes) which might be assigned to the strong side reaction caused by more defects in crystals of  $V_2O_5$ /graphene (4:1) sample.<sup>42</sup> Furthermore, three dominant cathodic peaks are missing in the 1<sup>st</sup> cycle for the  $V_2O_5$ -bm and hybrid electrodes which could be lower open circuit potential (OCP) of the cells during testing. After the electrode activation via the 1<sup>st</sup> cycle, the close overlap of the 2<sup>nd</sup>, 3<sup>rd</sup>, 4<sup>th</sup>, and 5<sup>th</sup> cycles indicates very good reversibility of the  $V_2O_5$ -bm,  $V_2O_5$ /graphene (2:1) and  $V_2O_5$ /graphene (4:1) electrodes.

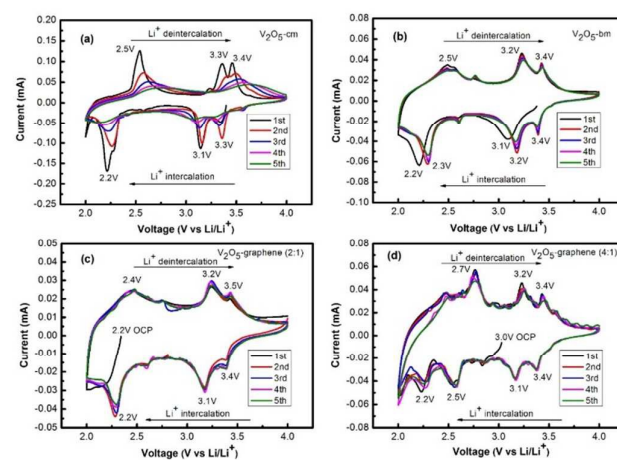


**Fig. 4** Cyclic voltammograms measured at a scan rate of  $0.05 \text{ mVs}^{-1}$  in the potential range of 4.0-2.0 V: (a)  $V_2O_5$ -cm; (b)  $V_2O_5$ -bm; (c) hybrid  $V_2O_5$ /graphene (2:1); and (d) hybrid  $V_2O_5$ /graphene (4:1).

Fig. 5 shows the first 5 cycles of discharge (Li intercalation) and charge (Li de-intercalation) curves of the electrodes in the potential window of 2.0-4.0 V at a current density of 0.5C. The shape of the discharge/charge curves of the three samples ( $V_2O_5$ -bm; hybrid  $V_2O_5$ /graphene (2:1); and hybrid  $V_2O_5$ /graphene (4:1)) is almost identical, where three main plateaus appear in each of the discharge and charge processes, corresponding to the electrochemical reactions among the transitional phases. The potential plateaus observed in the discharge/charge curves are

consistent with the three dominant redox peaks in the CV curves. However, shape of the discharge/charge curves for the  $V_2O_5$ -cm electrode is different from other electrodes and a potential polarization effect is significant in this electrode, which may be due to low conductivity and larger particle size of the sample. It is also clearly seen that 1<sup>st</sup> discharge capacity for both hybrid electrodes is lower than that of the subsequent discharge capacity. This indicates that the 1<sup>st</sup> Li intercalation in to the crystal is not as smooth as the subsequent Li intercalation because open circuit potential (OCP) was dramatically reduced for hybrid electrodes at the beginning of testing. After the 1<sup>st</sup> discharge, potential was increased significantly.

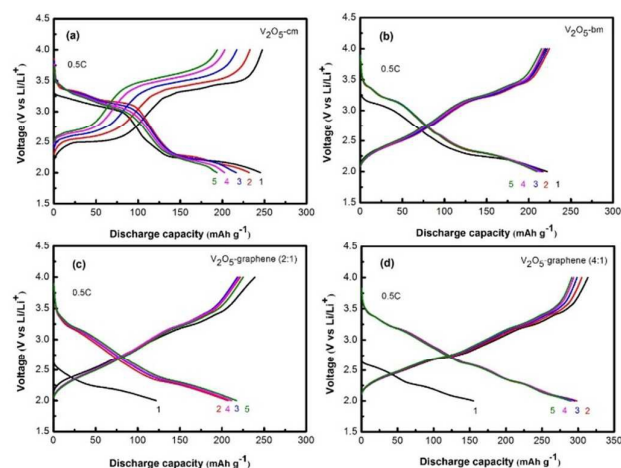


**Fig. 5** Galvanostatic discharge/charge potential profiles of (a)  $V_2O_5$ -cm; (b)  $V_2O_5$ -bm; (c) hybrid  $V_2O_5$ /graphene (2:1); and (d) hybrid  $V_2O_5$ /graphene (4:1) electrodes at 0.5C rate for the 1<sup>st</sup>, 2<sup>nd</sup>, 3<sup>rd</sup>, 4<sup>th</sup>, and 5<sup>th</sup> cycles.

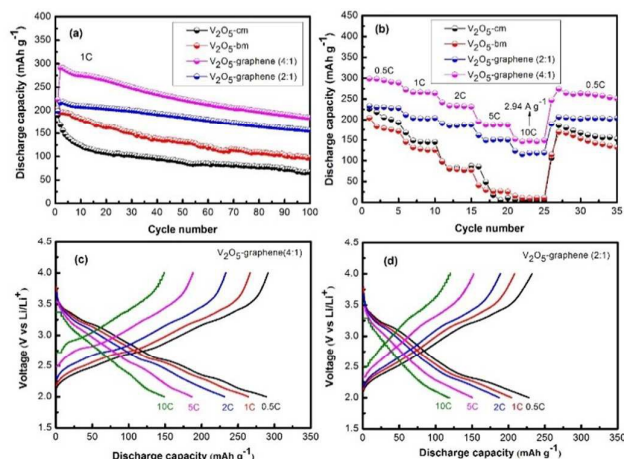
Cycling stability, rate performance and corresponding discharge/charge potential profiles for the electrodes are depicted in Fig. 6. The incorporation of *in-situ* graphene into the  $V_2O_5$  has an extraordinary effect on its electrochemical performance. Both hybrid electrodes exhibit good cycling stability with high discharge capacity of 185  $\text{mAh g}^{-1}$  (569  $\text{Wh kg}^{-1}$ ) for  $V_2O_5$ /graphene (4:1) and 157  $\text{mAh g}^{-1}$  (412  $\text{Wh kg}^{-1}$ ) for  $V_2O_5$ /graphene (2:1) at 1C after 100 cycles, respectively (Fig. 6 (a)). The achieved capacities are almost 63% for  $V_2O_5$ /graphene (4:1) electrode and 53 % for  $V_2O_5$ /graphene (4:1) electrode with respect to the theoretical capacity of 294  $\text{mAh g}^{-1}$ . It is important to note that graphene is not electrochemically active within the discharge-charge potential range of 2.0-4.0V and that the capacities are calculated based only on the weight of  $V_2O_5$  in the electrodes.<sup>43</sup> Capacity retention for hybrid electrodes is also commendable and it was approximately 64 % for  $V_2O_5$ /graphene (4:1) electrode and 73 % for  $V_2O_5$ /graphene (2:1) electrode with respect to the 2<sup>nd</sup> cycle discharge capacity. On the other hand, a significant capacity fading is observed for both  $V_2O_5$ -cm and  $V_2O_5$ -bm electrodes. The introduction of graphene also has a huge impact on the rate performance, which is a major issue for the electrodes without graphene ( $V_2O_5$ -cm and  $V_2O_5$ -bm).<sup>44</sup>

Fig. 6 (b) demonstrates a consecutive cycling performance at different current rates, measured after 5 cycles in ascending steps

from 0.5C to 10C, followed by a return to 0.5C. At fairly higher current densities, both hybrid electrodes still retain a high capacity. Discharge capacities are measured to be 289  $\text{mAh g}^{-1}$  (771  $\text{Wh kg}^{-1}$ ) at 0.5C, 264  $\text{mAh g}^{-1}$  (706  $\text{Wh kg}^{-1}$ ) at 1C, 232  $\text{mAh g}^{-1}$  (617  $\text{Wh kg}^{-1}$ ) at 2C, 187  $\text{mAh g}^{-1}$  (495  $\text{Wh kg}^{-1}$ ) at 5C and 149  $\text{mAh g}^{-1}$  (390  $\text{Wh kg}^{-1}$ ) at 10C for  $V_2O_5$ /graphene (4:1) electrode whereas it was 228  $\text{mAh g}^{-1}$  (597  $\text{Wh kg}^{-1}$ ) at 0.5C, 204  $\text{mAh g}^{-1}$  (534  $\text{Wh kg}^{-1}$ ) at 1C, 187  $\text{mAh g}^{-1}$  (488  $\text{Wh kg}^{-1}$ ) at 2C, 150  $\text{mAh g}^{-1}$  (387  $\text{Wh kg}^{-1}$ ) at 5C and 120  $\text{mAh g}^{-1}$  (303  $\text{Wh kg}^{-1}$ ) at 10C for  $V_2O_5$ /graphene (2:1) electrode, respectively. As the rate is back to 0.5C, discharge capacities of both  $V_2O_5$ /graphene (4:1) and  $V_2O_5$ /graphene (2:1) electrodes are still 253  $\text{mAh g}^{-1}$  (671  $\text{Wh kg}^{-1}$ ) and 203  $\text{mAh g}^{-1}$  (559  $\text{Wh kg}^{-1}$ ) even after 35 cycles, respectively. After 35 cycles, capacity recovery is calculated to be approximately 87 % (in respect to capacity of 289  $\text{mAh g}^{-1}$  obtained at 5th cycle at 0.5C initially) and 89 % (in respect to capacity of 228  $\text{mAh g}^{-1}$  obtained at 5th cycle at 0.5C initially) for  $V_2O_5$ /graphene (4:1) and  $V_2O_5$ /graphene (2:1) electrodes, respectively. However, rate capability of the electrodes (without graphene) is observed to be significantly hampered at the 10C rate and their capacities fade rapidly to below 10  $\text{mAh g}^{-1}$ .

Fig. 6 (c, d) further represent the potential profile of the first cycle for hybrid electrodes obtained at different current rates. Both hybrid electrodes still exhibit perfect discharge/charge characteristic shape which indicates that Li intercalation/deintercalation is quite similar among different current rates. However, such a huge improvement on rate performance, particularly at high rates (10C), suggests that *in-situ* incorporation of graphene in to  $V_2O_5$  crystals not only tremendously increases electronic conductivity (both interparticle and intraparticle conductivity) but also improves ionic conductivities of the hybrid electrodes. It is interesting to note that the content of graphene in the hybrid electrode plays a critical role on their electrochemical performance. Clearly, low content of graphene ( $V_2O_5$ /graphene (4:1) electrode) results in a higher discharge capacity at different current rates, while high content of ( $V_2O_5$ /graphene (2:1) electrode) leads to a lower discharge capacity, but much improved cycle stability (Fig. 6 (a, b)). It is anticipated that the lower graphene content may result in a better dispersion of the graphene sheets among the  $V_2O_5$  nanoparticles, while the higher graphene content may lead to the restacking of the graphene sheets.<sup>45</sup> It is also expected that thicker stacks of graphene could hold  $V_2O_5$  nanoparticles/aggregates tighter and, thus, maintain the structural integrity of the electrode during repeated cycling, consequently leading to a much better cycle life. Furthermore, higher graphene content may lead to more complete coverage over the  $V_2O_5$  nanoparticles/aggregates, which could help to hold the  $V_2O_5$  nanoparticles/aggregates together and prevent them from collapsing.<sup>33</sup>

considered as a key factor in improving the rate capability and cycling stability of the  $V_2O_5$ /graphene hybrid electrodes.



**Fig. 6** Electrochemical performances of the electrodes at 2-4V: (a) cycling stability up to 100 cycles at a current rate of 1C ( $1C = 294 \text{ mA g}^{-1}$ ); (b) rate capability at different current rates, ranging from low to moderate to very high; (c, d) potential profiles of the 5<sup>th</sup> cycle obtained at different current rates.

In order to gain insight into an improved performance of the hybrid electrodes and the structure-function relationship of the material, an EIS and *ex-situ* TEM characterization tests are conducted. Cycling stability and rate capability of the hybrid  $V_2O_5$ /graphene (2:1) and  $V_2O_5$ /graphene (4:1) electrodes are significantly superior to the electrodes made from other samples of  $V_2O_5$ -cm and  $V_2O_5$ -bm. These improvements originate from the *in-situ* generation of graphene and the role of this graphene host is quite obvious as it forms a conducting network resulting in more efficient electronic and ion transport in the electrode. The electrochemical impedance spectra of the  $V_2O_5$ -cm,  $V_2O_5$ -bm,  $V_2O_5$ /graphene (2:1) and  $V_2O_5$ /graphene (4:1) electrodes are shown in Fig. 7. In the spectrum, the inclined lines in the lower frequency region correspond to the Li diffusion process inside the electrode material and a semicircle in the medium-frequency region is related to the charge transfer resistance of the electrolyte and the electrode interface. The Nyquist plots in the medium frequency range clearly show that the diameters of the semicircles of hybrid electrodes are much smaller than that of the  $V_2O_5$ -cm and  $V_2O_5$ -bm electrodes, indicating that the hybrid electrodes provide much easier charge transfer at the electrode-electrolyte interface and, consequently, decrease the overall cell's internal resistance. The incorporation of graphene into  $V_2O_5$  by ball milling process significantly enhances the conductivity of the hybrid electrodes, since the graphene provides conductive paths in the vicinity of the  $V_2O_5$  particles, which is

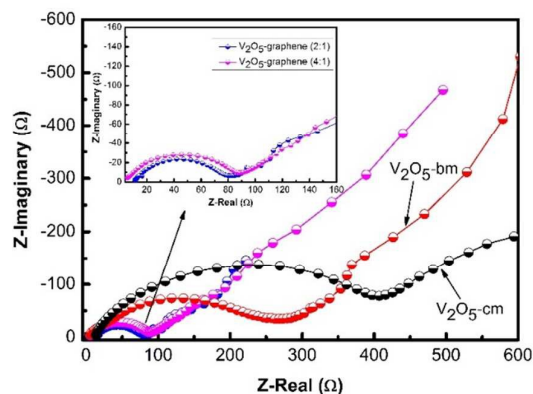


**Fig. 7** Electrochemical impedance spectra of the  $V_2O_5$ -cm,  $V_2O_5$ -bm,  $V_2O_5$ /graphene (2:1) and  $V_2O_5$ /graphene (4:1) electrodes.

Fig. 8 exhibits a post-cycling TEM and HRTEM investigations on the electrodes extracted after 100 cycles of galvanostatic discharge/charge at 1C. Fortunately, morphology of both hybrids remain well-preserved after intercalation/de-intercalation. Compared with the original morphology (Fig. 3 (c-f)),  $V_2O_5$  nanoparticles and aggregates still anchored with wrinkled graphene sheets (Fig. 8 (a, d)), demonstrating that the graphene networks effectively accommodate the volume variation during cycling and stabilize the whole electrode structure which ensure electron and ion transport in the electrode, simultaneously. The SAED patterns of the hybrid electrodes at charging to 4V are shown in Fig. 8 (b, e). The SAED patterns show a single component of  $V_2O_5$  (de-intercalated product) with *d* spacings of 0.334, 0.204, and 0.121 nm for  $V_2O_5$ /graphene (2:1) electrode which are well matched with crystallographic directions of (110), (051), and (033), respectively (Fig. 8 (b)). In the case of  $V_2O_5$ /graphene (4:1) electrode, it was 0.325, 0.196, and 0.117 nm which are well matched with crystallographic directions of (110), (051), and (172), respectively (Fig. 8 (e)). Fig. 8 (c, f) represent HRTEM images of the electrodes taken from the region of Fig. 8 (a, d), respectively. It is clearly observed that *in-situ* generated graphenes are composed of few layers with a *d* spacing of approximately 0.35 nm which is in good agreement with crystallographic direction of (002). Crystallinity of these graphenes is well retained even after cycling up to 100 cycles which represents high quality graphene. This observation clearly demonstrates the stability and robustness of this novel structure which is beneficial for self-expansion and self-shrinkage buffering and capable to accommodate structural strains and favour an enhanced cycling performance.

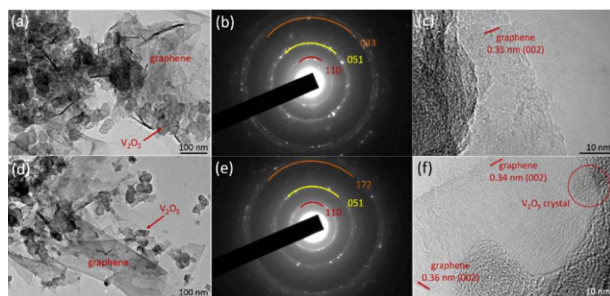


**Fig. 8** TEM investigation of the electrodes cycling up to 100 cycles at a current rate of 1C: Images (a-c) of hybrid  $V_2O_5$ /graphene (2:1) electrode: (a) a bright field TEM image; (b) corresponding SAED pattern; and (c) HRTEM image. Images (d-f) of hybrid  $V_2O_5$ /graphene (4:1) electrode: (d) a bright field TEM image; (e) corresponding SAED pattern; and (f) HRTEM image.

To further confirm the characteristic features and quality of graphene, Raman spectroscopy analysis was carried out for the  $V_2O_5$ /graphene hybrid electrodes. Fig. 9 (a, b) compares Raman spectroscopy between original materials (without cycling) and cycled electrodes. Both materials exhibit G-mode is at about  $1573\text{ cm}^{-1}$ , and is due to  $E_{2g}$  mode. G-band arises from the stretching of the C-C bond in graphitic materials, and is common to all  $sp^2$  carbon systems. Furthermore, both materials exhibit a strong peak in the range  $2500\text{--}2800\text{ cm}^{-1}$  in the Raman spectra which is a characteristic feature of  $sp^2$  carbon materials. Combined with the G-band, this spectrum is a Raman signature of graphitic  $sp^2$  materials and is called 2D-band. 2D-band is a second-order two-phonon process and exhibits a strong frequency dependence on the excitation laser energy. The 2D band can be used to determine the number of layer of graphene. This is mainly because in the multi-layer graphene, the shape of 2D band is pretty much different from that in the single-layer graphene. As shown in Fig. 9 (a, b), the 2D band is not much more intense and sharper as compared to the 2D band in the single layer graphene.<sup>46, 47</sup> Low intensity with a broader 2D band is consistent with the multi-layer feature of the graphene.

Overall, the  $V_2O_5$ /graphene hybrid electrode simultaneously demonstrates good cycling stability, excellent rate capability and high discharge capacity. Several factors might have contribution to enhance electrochemical performance of  $V_2O_5$ /graphene hybrid electrode which are discussed here.

(i) Although carbon materials cannot directly provide storage capacity for  $Li^+$  in the cathode, they can assist in improving the performance significantly. They are expected to improve the electrical conductivity and stability, and inhibit the agglomeration of

the cathode materials.<sup>48</sup> In this context, graphene is advantageous compared to other carbonaceous materials. Therefore, in the hybrid electrodes, graphene not only prevents aggregation of the intermediate and active materials but also provides good electrical contact with the particles which could reduce the polarization of the electrode. It is interesting to note that few-layer graphene can still be observed even after cycling the electrode (Fig. 8), which suggests that the graphene stacks are quite stable and can stabilize the whole electrode structure during cycling.

(ii)  $V_2O_5$ /graphene hybrid structure not only facilitates the kinetics for  $Li^+$  ion diffusion and electron transport by shortening the diffusion pathways to the nanoscale but also allows the most freedom for a change in dimension during lithium intercalation/de-intercalation.

(iii) In this hybrid structure, graphene not only serves as a matrix for  $V_2O_5$  nanoparticles, it also acts as a building block and establishes inimitable superstructures with interconnected networks; which is more helpful for the fast transportation of  $Li^+$  and therefore dramatically improve the performance of electrode materials.

(iv) The combined effect on electronic conduction and  $Li^+$  diffusion significantly improves the electrochemical performance.

These advantages result in a stable, high discharge capacity as well as an improved rate capability of the hybrid electrodes.

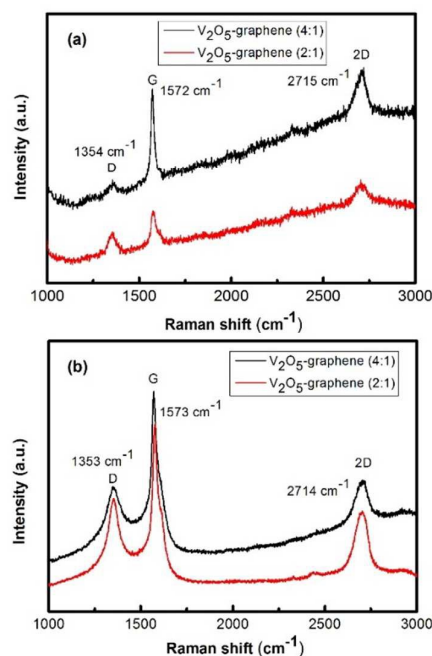


**Fig. 9** Room-temperature Raman spectra of  $V_2O_5$ /graphene hybrid samples: (a) original materials (without cycling) and (b) cycled electrodes after charging/discharging up to 100 cycles at 1C.

## Conclusions

To prevent the long-standing issues of low intrinsic electronic conductivity, slow lithium-ion diffusion and irreversible phase

transitions on deep discharge of  $V_2O_5$  electrode, a hybrid of  $V_2O_5$  nanostructured with graphene is proposed as cathode for lithium-ion batteries. Herein, a simple and low cost wet ball-milling method is used to create  $V_2O_5$ /graphene hybrid structure by *in-situ* mechanical peeling of bulk graphite and, simultaneously disperse them among  $V_2O_5$  nanoparticles/aggregates. The  $V_2O_5$ /graphene hybrid effectively leads to significant improvements in electronic conductivity, structural stability and ion diffusion, which in turn, results in excellent electrochemical performance. Low content of graphene results in a higher discharge capacity ( $185 \text{ mAh g}^{-1}$ ) at 1C rate, while high content of graphene leads to a lower discharge capacity ( $157 \text{ mAh g}^{-1}$ ), but much improved cycling stability. It is also demonstrated that this hybrid structure prevents self-aggregation of active materials and fully utilize the advantage of active materials.

### Acknowledgements

Financial support from Deakin University Higher Degree Research Scholarship and an Alfred Deakin Fellowship Award 2015 is acknowledged. Authors also acknowledge the support from Deakin Advanced Characterization Facility.

### Notes and references

- C. Zhang, Z. Chen, Z. Guo and X. W. Lou, *Energy Environ. Sci.*, 2013, **6**, 974.
- X.F. Zhang, K.-X. Wang, X. Wei and J.-S. Chen, *Chem. Mat.*, 2011, **23**, 5290.
- R. Alcantara, P. Lavela, J. Tirado, R. Stoyanova and E. Zhecheva, *J. Solid State Chem.*, 1997, **134**, 265.
- H. Huang, S.-C. Yin and L. S. Nazar, *Electrochem. Solid-State Lett.*, 2001, **4**, A170.
- Y. Yang, L. Li, H. Fei, Z. Peng, G. Ruan and J. M. Tour, *ACS Appl. Mater. Inter.*, 2014, **6**, 9590.
- M. S. Whittingham, *J. Electrochem. Soc.*, 1976, **123**, 315.
- D. Yu, C. Chen, S. Xie, Y. Liu, K. Park, X. Zhou, Q. Zhang, J. Li and G. Cao, *Energy Environ. Sci.*, 2011, **4**, 858.
- A. Pan, J.-G. Zhang, Z. Nie, G. Cao, B. W. Arey, G. Li, S.-q. Liang and J. Liu, *J. Mater. Chem.*, 2010, **20**, 9193.
- T. Zhai, H. Liu, H. Li, X. Fang, M. Liao, L. Li, H. Zhou, Y. Koide, Y. Bando and D. Golberg, *Adv. Mater.*, 2010, **22**, 2547.
- A. M. Cao, J. S. Hu, H. P. Liang and L. J. Wan, *Angew. Chem. Int. Ed. Engl.*, 2005, **44**, 4391.
- L. Mai, L. Xu, C. Han, X. Xu, Y. Luo, S. Zhao and Y. Zhao, *Nano Lett.*, 2010, **10**, 4750.
- Y. Wang, H. Li, P. He, E. Hosono and H. Zhou, *Nanoscale*, 2010, **2**, 1294.
- Y. Wang, Y. Wang, E. Hosono, K. Wang and H. Zhou, *Angew. Chem. Int. Ed. Engl.*, 2008, **47**, 7461.
- X. L. Wu, L. Y. Jiang, F. F. Cao, Y. G. Guo and L. J. Wan, *Adv. Mater.*, 2009, **21**, 2710.
- S.L. Chou, J.Z. Wang, J.Z. Sun, D. Wexler, M. Forsyth, H.K. Liu, D. R. MacFarlane and S.-X. Dou, *Chem. Mat.*, 2008, **20**, 7044.
- Y. Wang, K. Takahashi, K. Lee and G. Cao, *Adv. Funct. Mater.*, 2006, **16**, 1133.
- Y. S. Hu, X. Liu, J. O. Müller, R. Schlögl, J. Maier and D. S. Su, *Angew. Chem. Int. Ed. Engl.*, 2009, **48**, 210.
- G. Li, C. Zhang, H. Peng, K. Chen and *Macromol. Rapid Commun.*, 2009, **30**, 1841.
- Y. Wang, H. J. Zhang, W. X. Lim, J. Y. Lin and C. C. Wong, *J. Mater. Chem.*, 2011, **21**, 2362.
- B. Li, Y. Xu, G. Rong, M. Jing and Y. Xie, *Nanotechnology*, 2006, **17**, 2560.
- G. Li, C. Zhang, H. Peng and K. Chen, *Macromolecular rapid communications*, 2009, **30**, 1841.
- A. M. Glushenkov, V. I. Stukachev, M. F. Hassan, G. G. Kuvshinov, H. K. Liu and Y. Chen, *Crystal Growth & Design*, 2008, **8**, 3661.
- M. M. Rahman, A. Z. Sadek, I. Sultana, M. Srikanth, X. J. Dai, M. R. Field, D. G. McCulloch, S. B. Ponraj and Y. Chen, *Nano Res.*, 2015, **8**, 3591.
- Q. An, P. Zhang, Q. Wei, L. He, F. Xiong, J. Sheng, Q. Wang and L. Mai, *J. Mater. Chem. A*, 2014, **2**, 3297.
- X. Peng, X. Zhang, L. Wang, L. Hu, S. H. S. Cheng, C. Huang, B. Gao, F. Ma, K. Huo and P. K. Chu, *Adv. Funct. Mater.*, 2016, **26**, 784.
- M. Sathiyaa, A. Prakash, K. Ramesha, J. M. Tarascon and A. Shukla, *J. Am. Chem. Soc.*, 2011, **133**, 16291.
- H. Gwon, H.-S. Kim, K. U. Lee, D.-H. Seo, Y. C. Park, Y.-S. Lee, B. T. Ahn and K. Kang, *Energy Environ. Sci.*, 2011, **4**, 1277.
- H. Liu and W. Yang, *Energy Environ. Sci.*, 2011, **4**, 4000.
- M. Koltypin, V. Pol, A. Gedanken and D. Aurbach, *J. Electrochem. Soc.*, 2007, **154**, A605.
- C. H. Lui, L. Liu, K. F. Mak, G. W. Flynn and T. F. Heinz, *Nature*, 2009, **462**, 339.
- M. J. Allen, V. C. Tung and R. B. Kaner, *Chem. Rev.*, 2009, **110**, 132.
- K. Zhao, L. Zhang, R. Xia, Y. Dong, W. Xu, C. Niu, L. He, M. Yan, L. Qu and L. Mai, *Small*, 2016, **12**, 588.
- Q. Liu, Z.-F. Li, Y. Liu, H. Zhang, Y. Ren, C.-J. Sun, W. Lu, Y. Zhou, L. Stanciu and E. A. Stach, *Nat. Commun.*, 2015, **6**, 1.
- F. Carn, M. Morcrette, B. Desport and R. Backov, *Solid State Sci.*, 2013, **17**, 134.
- X.H. Xia, D.L.Chao, Y.Q.Zhang, Z.X.Shen and H.J.Fan, *Nano Today*, 2014, **9**, 785.
- M. Yi and Z. Shen, *J. Mater. Chem. A*, 2015, **3**, 11700.
- A. E. Del Rio-Castillo, C. Merino, E. Díez-Barra and E. Vázquez, *Nano Res.*, 2014, **7**, 963.
- P. Y. Liao, J. G. Duh, J. Fu. Lee and H. S. Sheu, *Electrochim. Acta*, 2007, **53**, 1850.
- G. Ali, J. H. Lee, S. H. Oh, B. W. Cho, K. W. Nam and K. Y. Chung, *ACS Appl. Mater. Interfaces*, 2016, **8**, 6032.
- A. Odani, V. G. Pol, S. V. Pol, M. Koltypin, A. Gedanken and D. Aurbach, *Adv. Mater.*, 2006, **18**, 1431.
- X. Rui, N. Ding, J. Liu, C. Li and C. Chen, *Electrochim. Acta*, 2010, **55**, 2384.
- K. E. Swider-Lyons, C. T. Love and D. R. Rolison, *Solid State Ionics*, 2002, **152-153**, 99.
- G. Du, K. H. Seng, Z. Guo, J. Liu, W. Li, D. Jia, C. Cook, Z. Liu and H. K. Liu, *RSC Advances*, 2011, **1**, 690.
- Z. F. Li, H. Zhang, Q. Liu, L. Sun, L. Stanciu and J. Xie, *ACS Appl. Mater. Inter.*, 2013, **5**, 2685.
- D. Chao, C. Zhu, X. Xia, J. Liu, X. Zhang, J. Wang, P. Liang, J. Lin, H. Zhang, Z. X. Shen and H. J. Fan, *Nano Lett.* 2015, **15**, 565.
- A. Ferrari, J. Meyer, V. Scardaci, C. Casiraghi, M. Lazzeri, F. Mauri, S. Piscanec, D. Jiang, K. Novoselov and S. Roth, *Phys. Rev. Lett.*, 2006, **97**, 187401.
- W. Zhao, M. Fang, F. Wu, H. Wu, L. Wang and G. Chen, *J. Mater. Chem.*, 2010, **20**, 5817.
- B. Sun, B. Wang, D. Su, L. Xiao, H. Ahn and G. Wang, *Carbon*, 2012, **50**, 727.

